ChemComm

COMMUNICATION

View Article Online
View Journal | View Issue

Cite this: *Chem. Commun.*, 2024, **60**, 9982

Received 6th June 2024,
Accepted 14th August 2024

DOI: 10.1039/d4cc02748e

rsc.li/chemcomm

Multimetal synergy in an iron–cobalt–nickel hydroxide electrocatalyst for electro-oxidative lignin depolymerization to produce value-added aromatic chemicals†

Pengfeng Li,[a] Jiaqi Zhang,[a] Shanshan Liu,[b] Fengcai Lei,[a] Xu Sun[c] and Junfeng Xie *[a]

A ternary iron–cobalt–nickel hydroxide nanoarray catalyst was fabricated, which achieves enhanced performance towards electro-oxidative depolymerization of lignin models to produce benzoic acid and phenol.

Lignin, one of the most abundant and sustainable natural materials, has been regarded as a promising resource for producing aromatic chemicals to reduce the dependence on fossil-derived feedstocks.[1–5] For instance, phenol and benzoic acid, the main available depolymerized aromatic chemicals, are widely used in synthetic fiber, resin, pharmaceuticals, agrochemicals and antiseptic industries.[6,7] Among various methods for converting lignin and their derivatives to such value-added aromatic chemicals, electro-oxidative lignin depolymerization (eLDP) is highly attractive owing to the high efficiency, soluble products and well-established reaction mechanism.[8–13] For instance, Cui and co-workers developed an efficient electrocatalyst with highly exposed atomically dispersed Pt–N_3C_1 sites, which leads to C–C bond cleavage in the lignin model to produce benzaldehyde and phenol with the aid of *tert*-butyl hydroperoxide.[10] Li's group designed a PbSnSb-based multiphase catalyst, which realized eLDP with the production of more than 16 kinds of aromatic compounds including phenols, aromatic hydrocarbon, ester, ketone, acid and aldehydes.[14] Unfortunately, currently explored electrocatalysts for eLDP are mainly based on noble metals or toxic elements such as Pt, Rh, RuO_2 and PbO_2,[15–17] which significantly limit their practical application. Recently, the rapid development of Earth-abundant electrocatalysts for the oxygen evolution reaction (OER) has shed light on the design of advanced eLDP catalysts.[18] The *in situ* formed hydroxyl radicals (•OH) during the anodic process could participate in eLDP and result in selective C–C bond cleavage with the formation of aromatic chemicals including benzoic acid and phenol.[8] For example, Duan's group proposed a Mn-doped CoOOH catalyst, which boosts the electro-oxidative C–C bond cleavage and converts lignin derivatives into various carboxylates.[8] Xu *et al.* designed a MoNiCoOOH catalyst *via* electrochemical reconstruction, which exhibits efficient eLDP behavior intermediated by *tert*-butyl hydroperoxide.[9] Focusing on this rising topic, herein we proposed a ternary iron–cobalt–nickel hydroxide nanoarray catalyst, which undergoes electrochemical reconstruction with the enrichment of high-valence metal sites. The multimetal synergy in the ternary FeCoNi-based catalyst could lead to enhanced electro-oxidation behavior, which guarantees facilitated reaction kinetics for the electro-oxidative depolymerization of the lignin model and endows the catalyst with high eLDP activity and good stability for highly selective production of value-added aromatic chemicals including benzoic acid and phenol.

In this work, we fabricated a nickel foam (NF)-supported ternary iron–cobalt–nickel hydroxide nanoarray catalyst (denoted as FeCoNi$(OH)_x$@NF) *via* a mild hydrothermal route (Experimental section S1, ESI†). To investigate the multimetal synergy for eLDP catalysis, binary CoNi$(OH)_x$@NF and unary $Co(OH)_2$@NF were prepared for comparison. X-ray diffraction (XRD) was used to obtain the structural information. As shown in Fig. 1A, the intensive diffraction peaks corresponding to nickel (JCPDS card no. 87-0712) can be identified, which originate from the NF skeleton. Notably, two weak peaks emerge in the low-angle region, indicating the formation of a lamellar structure corresponding to FeCoNi$(OH)_x$. In addition, a similar layered structure of CoNi$(OH)_x$@NF and $Co(OH)_2$@NF can be identified from the XRD patterns in Fig. S1 (ESI†).

[a] *College of Chemistry, Chemical Engineering and Materials Science, Key Laboratory of Molecular and Nano Probes (Ministry of Education), Collaborative Innovation Center of Functionalized Probes for Chemical Imaging in Universities of Shandong, Shandong Normal University, Jinan, Shandong, 250014, P. R. China. E-mail: xiejf@sdnu.edu.cn*

[b] *College of Chemical Engineering and Safety, Shandong University of Aeronautics, Binzhou, Shandong, 256603, P. R. China*

[c] *Key Laboratory of Interfacial Reaction & Sensing Analysis in Universities of Shandong, School of Chemistry and Chemical Engineering, University of Jinan, Jinan 250022, Shandong, P. R. China*

† Electronic supplementary information (ESI) available: Experimental section and additional characterization details. See DOI: https://doi.org/10.1039/d4cc02748e

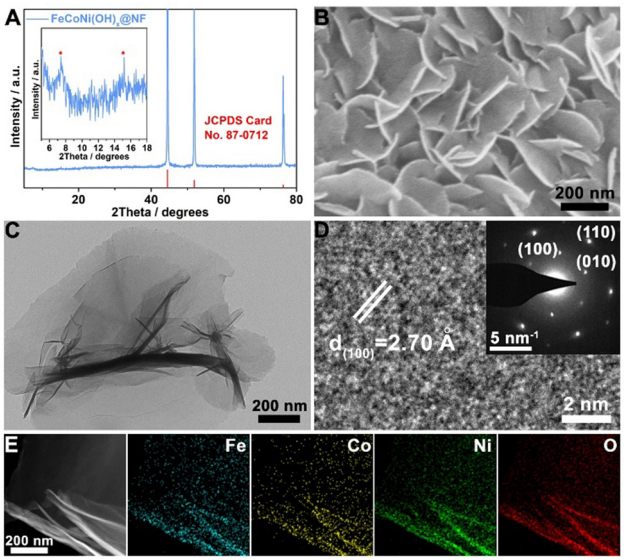

Fig. 1 (A) XRD pattern of FeCoNi(OH)$_x$@NF. Inset shows the enlarged region with a characteristic lamellar structure. (B) and (C) SEM and TEM images. (D) HRTEM image and SAED pattern of the detached FeCoNi(OH)$_x$ nanosheets. (E) HAADF-STEM and elemental maps.

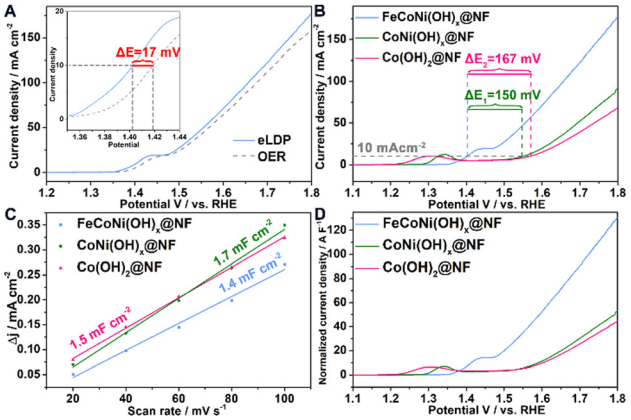

Fig. 2 (A) LSV curves of FeCoNi(OH)$_x$@NF for eLDP and the OER. (B) eLDP performance of various catalysts. (C) Evaluation of C_{dl} values. (D) C_{dl}-normalized eLDP activity.

Scanning electron microscopy (SEM) and transmission electron microscopy (TEM) were used to study the morphology of the catalysts. As shown in Fig. 1B and C, uniform nanoarrays with vertically grown nanosheets can be identified for FeCoNi(OH)$_x$@NF, and a similar morphology can be confirmed for CoNi(OH)$_x$@NF and Co(OH)$_2$@NF in Fig. S2 and S3 (ESI†), respectively. The high-resolution TEM (HRTEM) image in Fig. 1D reveals the lattice fringes with a d-spacing of 2.70 Å, which correspond to the (100) facets of hydroxide. The selected area electron diffraction (SAED) pattern in the inset of Fig. 1D clearly reveals a typical six-fold symmetry, confirming the single-crystalline feature of the ternary hydroxide nanosheets. In addition, high-angle annular dark-field scanning transmission electron microscopy (HAADF-STEM) and elemental mapping analyses are shown in Fig. 1E, from which homogeneous distribution of Fe, Co, Ni, and O can be confirmed. X-ray photoelectron spectroscopy (XPS) was further applied to study the valence information of FeCoNi(OH)$_x$@NF. As shown in Fig. S4 (ESI†), Fe^{3+} is dominating for iron, while mixed valence of $Co^{2+/3+}$ and $Ni^{2+/3+}$ can be confirmed. The local high-valence Fe^{3+}, Co^{3+} and Ni^{3+} species could directly serve as the active sites for a series of electro-oxidation reactions,[19–21] which may be beneficial to boost the electro-oxidative lignin depolymerization.

To investigate the catalytic activity and figure out the multimetal synergy in electro-oxidative depolymerization of the lignin model, a three-electrode setup was built, where the self-supported catalyst served as the working electrode and a mixed solution of acetonitrile-water ($V_{MeCN}:V_{H_2O}$ = 1 : 4) with 1 g L^{-1} lignin model with characteristic β-*O*-4 linkage (2-phenoxy-1-phenylethanol) and 0.5 M KOH was used as the electrolyte. The linear sweeping voltammetry (LSV) curves in Fig. 2A indicate that the addition of the lignin substrate could reduce the required potential at specific current density. For example, the potential at 10 mA cm^{-2} eLDP current density is measured to be 1.402 V *vs.* RHE, which is 17 mV lower than that for the OER. This indicates that even the eLDP process with sluggish reaction kinetics could also reduce the overall potential and save energy for the coupled hydrogen production compared with the OER‖HER cell.

Fig. 2B reveals the eLDP performance of the catalysts with different compositions. As can be seen, the ternary FeCoNi(OH)$_x$@NF catalyst displays much higher activity than binary CoNi(OH)$_x$@NF and unary Co(OH)$_2$@NF. The required potential of FeCoNi(OH)$_x$@NF for achieving a 10 mA cm^{-2} current density is 150 mV lower than that of the binary catalyst and 167 mV lower than that of unary Co(OH)$_2$@NF. That is, as the number of metallic element increases, the eLDP activity is significantly enhanced, thereby demonstrating the multimetal synergy in boosting lignin electro-oxidation. To go further, the current density of FeCoNi(OH)$_x$@NF at 1.6 V *vs.* RHE reaches 71.0 mA cm^{-2}, while low values of 19.4 and 14.5 mA cm^{-2} are obtained for CoNi(OH)$_x$@NF and Co(OH)$_2$@NF, displaying roughly 4 and 5 times enhancement, respectively.

Electrochemical impedance spectroscopy (EIS) was used to investigate the reaction kinetics of the catalysts during the eLDP process. As shown in Fig. S5 (ESI†), FeCoNi(OH)$_x$@NF exhibits a small charge transfer resistance (R_{ct}) of 10.1 Ω, which is much smaller than that of CoNi(OH)$_x$@NF (116.0 Ω) and Co(OH)$_2$@NF (202.0 Ω). The small R_{ct} of the ternary catalyst may arise from the multimetal synergy that optimizes the intrinsic electronic structure and boost the charge transfer.[21] The electrochemical surface area (ECSA) of the catalysts was evaluated by measuring the electrochemical double-layer capacitances (C_{dl}, methods can be seen in Fig. S6 (ESI†) and related discussions). As shown in Fig. 2C, the ternary, binary and unary catalysts display similar C_{dl} values of 1.4, 1.7 and 1.5 mF cm^{-2}, which is consistent with the similar nanosheet array morphology. Hence, ECSA is not the dominating factor that determines the eLDP activity. We further conducted performance normalization of the LSV curves using the corresponding C_{dl} values to figure out the difference in intrinsic activity.[22] As revealed in Fig. 2D, FeCoNi(OH)$_x$@NF still exhibits the highest activity among the tested catalysts, where a large C_{dl}-normalized

current density ($j_{C_{dl}}$) of 53.0 A F^{-1} can be achieved at 1.6 V *vs.* RHE, showing roughly 5- and 6-fold enhancement compared to the binary and unary counterparts, respectively. The large $j_{C_{dl}}$ of FeCoNi(OH)$_x$@NF confirms the excellent intrinsic activity towards eLDP, which can be attributed to the multimetal synergy with enriched high-valence active sites.

The cleavage products of lignin model during eLDP were analyzed by means of gas chromatography–mass spectrometry (GC-MS) and nuclear magnetic resonance (NMR). As shown in Fig. S7–S11 (ESI†), both GC-MS and NMR results of the electrolyte after catalysis by FeCoNi(OH)$_x$@NF indicate the formation of benzoic acid, phenol and formate during eLDP, suggesting the effective depolymerization of the lignin model. To further evaluate the eLDP behavior of the composition-modulated catalysts, quantitative analysis of the aromatic products (*i.e.*, benzoic acid and phenol) was conducted. As can be seen in Fig. 3A, after 5 h of eLDP catalysis at 1.5 V *vs.* RHE, the ternary FeCoNi(OH)$_x$@NF catalyst displays much higher performance in producing benzoic acid and phenol than the counterparts. In detail, the conversion rate of the lignin model reaches 49.6%, and the yields of benzoic acid and phenol are as high as 31.5% and 14.2%, respectively. When applying a lower potential of 1.42 V *vs.* RHE to suppress the competitive OER, the conversion rate of the lignin model increases to 51.5%, and the yields of benzoic acid and phenol increase to 35.9% and 34.1%, respectively (Fig. 3B). In contrast, the binary and unary catalysts display negligible eLDP activity at such a low potential, further demonstrating the high eLDP performance of the ternary FeCoNi(OH)$_x$@NF catalyst for producing value-added aromatic chemicals.

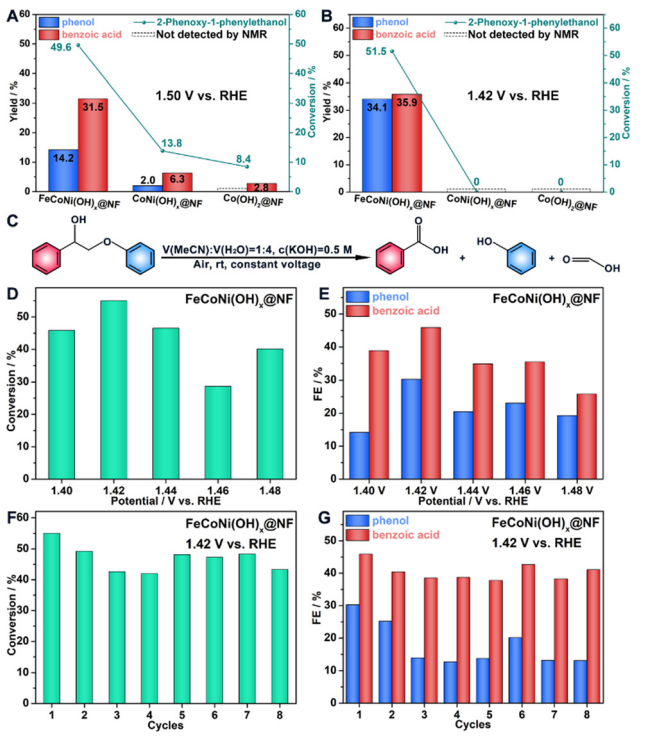

Fig. 3 (A) and (B) Conversion rate and yield of the aromatic products catalyzed by various catalysts at specific potential. (C) Schematic diagram of the eLDP process. (D) and (E) Conversion rate and faradaic efficiency at different potentials. (F) and (G) Cycling performance of FeCoNi(OH)$_x$@NF for conversion rate and faradaic efficiency.

The electro-oxidative depolymerization pathway of the lignin model can be described in Fig. 3C, and the required quantity of electric charge is determined to be 13.51C. Potentials lower than 1.5 V *vs.* RHE and theoretical quantity of electric charge were selected to quantitatively analyze the lignin upgrading behavior of the ternary FeCoNi(OH)$_x$@NF catalyst. As shown in Fig. 3D, a satisfied conversion rate can be achieved in the range of 1.4–1.48 V *vs.* RHE, and the conversion rate at 1.42 V *vs.* RHE reaches a top value of 55.0%. In addition, as revealed in Fig. 3E, the faradaic efficiency (FE) of the aromatic products displays a similar trend to the conversion rate, where high FEs of 45.9% and 30.3% can be identified for benzoic acid and phenol, respectively. The high conversion rate and FEs demonstrate the excellent eLDP activity of the ternary FeCoNi(OH)$_x$@NF catalyst, which could effectively convert the lignin model to value-added aromatic chemicals.

We further conducted cycling tests of the ternary FeCoNi(OH)$_x$@NF catalyst to evaluate the operational stability towards continuous eLDP. Eight sequential cycles with theoretical quantity of electric charge were performed at the optimal potential of 1.42 V *vs.* RHE. As shown in Fig. 3F, the conversion rate of the lignin model displays slight decrement as the cycling proceeds, and a satisfied conversion rate in the range of 42.0–49.3% can still be resulted. The FEs of benzoic acid and phenol also confirm the good operational stability. As revealed in Fig. 3G, the FEs of benzoic acid and phenol of the 8th cycle were calculated to be 41.1% and 13.1%, respectively. The decreased FE of phenol may arise from further oxidation with the generation of benzoquinone.

Post-catalytic characterization after eight eLDP cycles was conducted to survey the possible change of the ternary FeCoNi(OH)$_x$@NF catalyst. As revealed in the TEM image in Fig. S12 (ESI†), the nanosheet morphology of the ternary catalyst was well maintained, and obviously increased surface roughness can be identified, suggesting the surface reconstruction that leads to the enrichment of active sites.[23–25] Fig. S13 (ESI†) further gives the structural information of FeCoNi(OH)$_x$@NF after long-term eLDP. The HRTEM image and SAED pattern indicate the emerging orthorhombic α-MOOH phase (JCPDS card no. 27-0956) with characteristic (101), (210) and (310) facets, further confirming the occurrence of the electrochemical pre-oxidation process that causes the formation and stabilization of the high-valence active species. In addition, the elemental mapping analysis in Fig. S14 (ESI†) demonstrates the homogenous distribution of Fe, Co, Ni and O, indicating the retention of the ternary feature. Post-catalytic XPS analysis in Fig. S15 (ESI†) also confirms the well retained metallic elements. Of note, apart from the dominating Fe^{3+} in both fresh and used catalysts, the components of Co^{3+} and Ni^{3+} increase remarkably along with the eLDP operation. As listed in Fig. S16 (ESI†), after eight sequential eLDP cycles, the Co^{3+}/Co^{2+} ratio increases from 0.67 to 1.86, while the Ni^{3+}/Ni^{2+} ratio increases from 0.47 to 0.61, thereby confirming the enrichment of the catalytically active high-valence species that favor the eLDP catalysis.

According to the experimental results and previous literature,[8] the electro-oxidative depolymerization of the lignin model

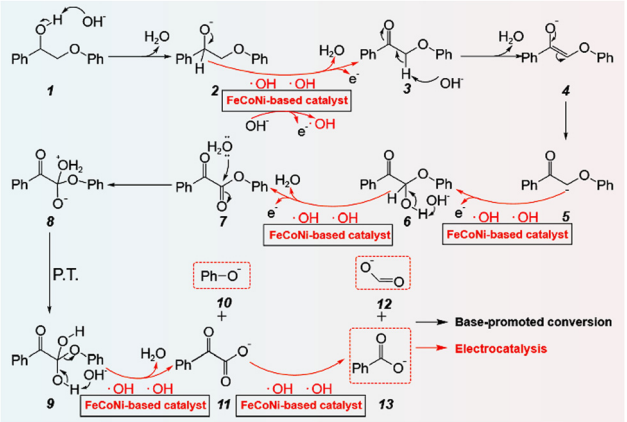

Fig. 4 Proposed reaction pathways of eLDP catalyzed by the ternary FeCoNi(OH)$_x$@NF catalyst.

involves a multi-step reaction pathway. As revealed in Fig. 4, 2-phenoxy-1-phenylethanol (**1**) is deprotonated by alkali catalysis to become a more reactive alkoxide **2**. Then, alkoxide **2** can be oxidized by electrophilic hydroxyl radicals (•OH) which are electrocatalytically formed on the surface of the ternary catalyst, undergoing H elimination to obtain ketone **3**. After that, hydroxide ions induce keto–enol tautomerization of **3** to generate enol **4** *via* a carbanion intermediate. Then, nucleophilic attack of the carbanion intermediate **5** to electrophilic •OH on the surface of FeCoNi(OH)$_x$@NF leads to the generation of α-ketone **6**. Subsequently, **6** is electro-oxidized on the surface of the catalyst to form ketone **7**, and immediately undergoes an addition reaction with water to produce **8** and then forms **9** *via* proton transfer (P.T.). After that, with the aid of •OH, **9** eliminates phenolate (**10**) to form **11**. Finally, carbon–carbon bond cleavage occurs, resulting in the formation of formate (**12**) and benzoate (**13**). Overall, value-added aromatic chemicals (benzoic acid and phenol) can be obtained from the electro-oxidative depolymerization of the lignin model, and the hydroxyl radicals *in situ* formed on the surface of the ternary catalyst are crucial for such a valorization process.

In this work, we fabricated a ternary FeCoNi hydroxide nanoarray catalyst, which exhibits efficient performance towards electro-oxidative lignin depolymerization to produce benzoic acid and phenol. The multimetal synergy of the ternary catalyst could lead to significantly improved electro-oxidation behavior towards the depolymerization of the lignin model compared with the binary and unary catalysts. At an optimal potential of 1.42 V *vs.* RHE, efficient and stable conversion from the lignin model to value-added aromatic chemicals (benzoic acid and phenol) can be achieved with a high conversion rate and faradaic efficiency. Besides, the catalyst evolution during long-term eLDP operation was investigated, and the reaction mechanism was further proposed. Although direct depolymerization of raw lignin is of great challenge owing to its complex linkage types and difficulty in mass transfer, this work could still shed light on catalyst design for selective electro-oxidative linkage breaking and will guide the design of lignin upgrading catalysts in near future.

This work was supported by the National Natural Science Foundation of China (22171167) and the Talent Introduction and Training Program for Youth Innovation Teams in Colleges and Universities of Shandong Province.

Data availability

The data supporting this article have been included as part of the ESI.†

Conflicts of interest

There are no conflicts to declare.

References

1 A. J. Ragauskas, G. T. Beckham, M. J. Biddy, R. Chandra, F. Chen, M. F. Davis, B. H. Davison, R. A. Dixon, P. Gilna, M. Keller, P. Langan, A. K. Naskar, J. N. Saddler, T. J. Tschaplinski, G. A. Tuskan and C. E. Wyman, *Science*, 2014, **344**, 1246843.
2 Z. Luo, C. Liu, A. Radu, D. F. de Waard, Y. Wang, J. T. Behaghel de Bueren, P. D. Kouris, M. D. Boot, J. Xiao, H. Zhang, R. Xiao, J. S. Luterbacher and E. J. M. Hensen, *Nat. Chem. Eng.*, 2024, **1**, 61–72.
3 C. Li, X. Zhao, A. Wang, G. W. Huber and T. Zhang, *Chem. Rev.*, 2015, **115**, 11559–11624.
4 E. Subbotina, T. Rukkijakan, M. D. Marquez-Medina, X. Yu, M. Johnsson and J. S. M. Samec, *Nat. Chem.*, 2021, **13**, 1118–1125.
5 X. Zeng, Y. Qi, X. Lin, S. Li and Y. Qin, *Chem. Eng. Sci.*, 2024, **288**, 119798.
6 W. Xiong, Q. Shi and W. H. Liu, *J. Am. Chem. Soc.*, 2022, **144**, 15894–15902.
7 Z. Li, Y. Yan, S.-M. Xu, H. Zhou, M. Xu, L. Ma, M. Shao, X. Kong, B. Wang, L. Zheng and H. Duan, *Nat. Commun.*, 2022, **13**, 147.
8 H. Zhou, Z. Li, S.-M. Xu, L. Lu, M. Xu, K. Ji, R. Ge, Y. Yan, L. Ma, X. Kong, L. Zheng and H. Duan, *Angew. Chem., Int. Ed.*, 2021, **60**, 8976–8982.
9 J. Xu, J. Meng, Y. Hu, Y. Liu, Y. Lou, W. Bai, S. Dou, H. Yu and S. Wang, *Research*, 2023, **6**, 0288.
10 T. Cui, L. Ma, S. Wang, C. Ye, X. Liang, Z. Zhang, G. Meng, L. Zheng, H.-S. Hu, J. Zhang, H. Duan, D. Wang and Y. Li, *J. Am. Chem. Soc.*, 2021, **143**, 9429–9439.
11 Y. Qi, B. Liu, X. Qiu, X. Zeng, Z. Luo, W. Wu, Y. Liu, L. Chen, X. Zu, H. Dong, X. Lin and Y. Qin, *Adv. Mater.*, 2023, **35**, 2208284.
12 K. Wang, Z. Guo, M. Zhou, Y. Yang, L. Li, H. Li, R. Luque and S. Saravanamurugan, *J. Energy Chem.*, 2024, **91**, 542–578.
13 L. Ma, H. Zhou, X. Kong, Z. Li and H. Duan, *ACS Sustainable Chem. Eng.*, 2021, **9**, 1932–1940.
14 Y. Jia, Y. Wen, X. Han, J. Qi, Z. Liu, S. Zhang and G. Li, *Catal. Sci. Technol.*, 2018, **8**, 4665–4677.
15 M. Garedew, C. H. Lam, L. Petitjean, S. Huang, B. Song, F. Lin, J. E. Jackson, C. M. Saffron and P. T. Anastas, *Green Chem.*, 2021, **23**, 2868–2899.
16 P. Cai, H. Fan, S. Cao, J. Qi, S. Zhang and G. Li, *Electrochim. Acta*, 2018, **264**, 128–139.
17 T. Peng, W. Zhang, B. Liang, G. Lian, Y. Zhang and W. Zhao, *Nat. Commun.*, 2023, **14**, 7229.
18 J. Song, C. Wei, Z.-F. Huang, C. Liu, L. Zeng, X. Wang and Z. J. Xu, *Chem. Soc. Rev.*, 2020, **49**, 2196–2214.
19 L. Kang, J. Li, Y. Wang, W. Gao, P. Hao, F. Lei, J. Xie and B. Tang, *J. Colloid Interface Sci.*, 2023, **630**, 257–265.
20 J. Xie, J. Xin, R. Wang, X. Zhang, F. Lei, H. Qu, P. Hao, G. Cui, B. Tang and Y. Xie, *Nano Energy*, 2018, **53**, 74–82.
21 C. Dong, M. Guo, W. Gao, P. Hao, F. Lei, J. Xie and B. Tang, *J. Colloid Interface Sci.*, 2022, **627**, 891–899.
22 J. Xie, S. Li, X. Zhang, J. Zhang, R. Wang, H. Zhang, B. Pan and Y. Xie, *Chem. Sci.*, 2014, **5**, 4615–4620.
23 W. Sun, J. Li, W. Gao, L. Kang, F. Lei and J. Xie, *Chem. Commun.*, 2022, **58**, 2430–2442.
24 L. Gao, X. Cui, C. D. Sewell, J. Li and Z. Lin, *Chem. Soc. Rev.*, 2021, **50**, 8428–8469.
25 M. Hao, J. Chen, J. Chen, K. Wang, J. Wang, F. Lei, P. Hao, X. Sun, J. Xie and B. Tang, *J. Colloid Interface Sci.*, 2023, **642**, 41–52.